

Global Biogeochemical Cycles

Supporting Information for

Pacific anthropogenic carbon between 1991 and 2017

Carter, B.R.^{1,2}, Feely, R.A.², Wanninkhof, R.³, Kouketsu, S.⁴, Sonnerup, R.E.¹, Pardo, P.C.⁵, Sabine C.L.⁶,
Johnson, G. C.², Sloyan, B.M.⁷, Murata, A.⁴, Mecking, S.⁸, Tilbrook, B.⁹, Speer, K.^{9,10}, Talley, L.D.¹¹, Millero,
F.J.¹², Wijffels, S.E.^{7,12}, Macdonald, A.M.¹³, Gruber, N.¹⁴, Bullister, J. L.^{2,15}

¹Joint Institute for the Study of the Atmosphere and Ocean, University of Washington, 3737 Brooklyn
Ave., Seattle, WA, 98115

²Pacific Marine Environmental Laboratory, National Oceanic and Atmospheric Administration, 7600 Sand
Point Way, NE, Seattle, WA, 98115

³Atlantic Oceanographic and Meteorological Laboratory, National Oceanic and Atmospheric
Administration, Miami, FL, 33149

⁴Japan Agency for Marine-Earth Science and Technology (JAMSTEC), 2-15 Natsushima-cho, Yokosuka,
Kanagawa, Japan

⁵Antarctic Climate and Ecosystem Cooperative Research Center, University of Tasmania, Hobart,
Tasmania

⁶SOEST, University of Hawaii Manoa, 1000 Pope Rd., Honolulu, HI 96822

⁷CSIRO Oceans and Atmosphere, Castray Esplanade, Hobart, TAS, Australia 7000

⁸Applied Physics Laboratory, University of Washington, Seattle, Washington, USA

⁹Commonwealth Scientific and Industrial Research Organisation (CSIRO) Marine Research and Antarctic
Climate and Ecosystem Cooperative Research Center, Hobart, Tasmania 7001, Australia.

¹⁰Department of Oceanography, The Florida State University, Tallahassee, Florida

¹¹ Scripps Institution of Oceanography, University of California, San Diego, La Jolla, California, USA

¹²Rosenstiel School of Marine and Atmospheric Science, University of Miami, Coral Gables, Florida, USA

¹³Woods Hole Oceanographic Institution, Woods Hole, Massachusetts, USA

¹⁴Environmental Physics, Institute of Biogeochemistry and Pollutant Dynamics, ETH Zurich, Zurich,
Switzerland

¹⁵Deceased

32 **Contents of this file**

33 Supporting text S1, S2, and S3.

34 Supplementary Figures S1, S2, S3, S4, S5

35 Supplementary Table S1, S2, S3

36

37 **Additional Supporting Information (Files uploaded separately)**

38 CruiseInformation.xlsx

39 PacBasinCanth.gif

40 PacBasinDeltapH.gif

41 PacBasinDeltaOmega.gif

42

43 **Introduction**

44 The supplementary materials are intended to accomplish several tasks:

45 Text S1: provides the uncertainty assessment and method comparison.

46 Text S2: provides a detailed list of steps in the various methods used.

47 Text S3: provides additional methods details for the transport matrix C_{anth} storage simulation.

48 Figure S1: Referenced by Text S3.

49 Figure S2: Successive-occupation C_{anth} accumulation rate estimates derived by comparing subsequent
50 pairs of repeated sections occupations that were not presented in the main text. This is provided for
51 readers interested in sections that are not discussed in the text.

52 Figure S3: Changes in successive occupation C_{anth} accumulation rates for the sections in Fig. 7, referenced
53 in the main text.

54 Figure S4: Changes in accumulation along zonal bands, as referenced in the main text.

55 Figure S5: Provides vertical context for the basin inventory estimates, and is briefly mentioned in the
56 main text.

57 Table S1: Referenced in Text S1. Part of an explanation of how uncertainty was estimated.

58 Table S2: Referenced in Text S1. Provides uncertainty estimates for many methods.

59 Table S3: Referenced in Text S2. Important for method reproducibility.

60 Additional Supporting Information: CruiseInformation.xlsx contains cruise-specific information (e.g.
61 Expocodes).

62 Additional Supporting Information: Finally, the “Additional Supporting Information” files provide .gif
63 animations of C_{anth} estimates and the impacts of C_{anth} on pH (ΔpH) and aragonite saturation state ($\Delta\Omega$)
64 along the 14 sections considered from 1995 to 2017. These estimates are obtained with a significant
65 amount of interpolation and (at times) extrapolation over time. They therefore have even larger (and
66 uncharacterized) uncertainties than any of the estimates presented within the manuscript. These are
67 intended to be used as simple visualizations and teaching aids for the accumulation of C_{anth} and its
68 impacts.

69 **Text S1: Method uncertainty assessment and comparison**

70 Here we test many combinations of methods discussed. This analysis is presented primarily to show that
71 the new methods are at least as, or more, skillful as other variants. The test for these methods is nearly
72 identical to the test used for *Carter et al.* [2017b]’s Appendix B. The test relies on model output from two
73 Earth System Model simulations. Both simulations use the ESM2M model with TOPAZ biogeochemistry
74 [*Dunne et al.*, 2012, 2013] which includes parameterizations for denitrification, among many other
75 processes. The physical circulation and freshwater exchange patterns of the two simulations are set to be
76 identical and the only difference in forcing between the two runs is that one simulation has a constant
77 preindustrial atmospheric $p\text{CO}_2$ while the other experiences the historical $p\text{CO}_2$ transient. This setup
78 affords a simple test case where the anthropogenic CO_2 impact on DIC is exactly the DIC difference
79 between the simulations. The 1995 to 2005 C_{anth} accumulation is then used to test the performance of
80 various MLR approaches along 5 meridional sections at 79.5°E, 59.5°E, 179.5°E, 95.5°W, and 24.5°W.
81 These tests are repeated for simulations both with and without random (unique for each property value)
82 and systematic (section-wide) offsets that were applied to the model output to simulate observing errors.
83 These offsets are selected randomly from a normally distributed population with standard deviations
84 equaling the values indicated in Table S1. We interpret the adjustment thresholds of *Olsen et al.* [2016] as
85 $\sim 2\sigma$ confidence intervals, and therefore estimate these standard deviations as values that add in
86 quadrature to approximately half of the values they choose. Generally, repeat hydrographic cruises are
87 assumed to produce data with low uncertainties (e.g. $< 2 \mu\text{mol kg}^{-1}$ DIC [*Key et al.*, 2010]). Each section
88 was tested only once without simulated measurement errors ($n=5$ total), 5 times with only simulated
89 random offsets ($n=25$), 5 times with only simulated systematic offsets ($n=25$), and 20 times with both
90 random and systematic simulated measurement errors ($n=100$ total). The simulated errors were identical
91 for all method variants tested in each of the trials with errors. Statistics were generated for the uncertainty
92 estimates with both types of simulated errors by bootstrapping uncertainty estimates from many (100)
93 combinations of 25 randomly selected trials from the 100 trials. We assumed 4 degrees of freedom when
94 calculating confidence intervals for these uncertainties (Table S2).

95

Table S1. Standard deviations (σ) of normally distributed populations from which random and systematic offsets were selected. These offsets were applied to model outputs to simulate measurement uncertainties.

Property	DIC	A_T	N	P	Si	O_2	T	S
Units	$\mu\text{mol kg}^{-1}$	$^{\circ}\text{C}$						
Random Offset σ	2	2	0.1	0.01	0.1	1	0.002	0.002
Systematic Offset σ	1	2	0.4	0.04	0.4	1	0.01	0.01

96

Table S2. Tested eMLR variants, their average absolute biases (AAB), and root-mean-squared errors (RMSE), with and without random measurement errors and consistent measurement offsets of the magnitudes indicated in Table S1. All values are in $\mu\text{mol kg}^{-1} C_{\text{anth}}$ errors over a 10 year span. $\mathbf{T}^{\wedge}\mathbf{W}_2$

is used for this analysis. Bootstrapped 95% confidence intervals on mean uncertainties are given for the estimates with both simulated uncertainties.

Variant	AAB	RMSE	AAB	RMSE	AAB	RMSE	AAB	RMSE
	<i>No added errors</i>		<i>Random offsets only</i>		<i>Systematic offsets only</i>		<i>Both offset types (best estimate of uncertainty)</i>	
E*	0.26	2.38	0.24	2.42	2.23	3.67	2.0 ±0.1	3.4 ±0.1
E^X	0.26	2.39	0.24	2.43	2.21	3.67	2.0 ±0.1	3.5 ±0.1
T*W₂	0.20	2.32	0.24	2.36	2.14	3.48	1.9 ±0.1	3.3 ±0.1
E^{&}	0.25	2.36	0.23	2.41	1.86	3.38	1.9 ±0.1	3.4 ±0.1
T^{&}	0.19	2.31	0.22	2.36	1.85	3.34	1.9 ±0.1	3.25 ±0.09
T^{&}W₂	0.18	2.31	0.23	2.35	1.77	3.21	1.8 ±0.1	3.27 ±0.09
B	0.58	3.09	0.55	3.03	1.86	4.52	1.8 ±0.1	4.38 ±0.09
E	0.57	2.74	0.54	2.75	1.57	3.44	1.5 ±0.1	3.38 ±0.05
W	0.59	2.74	0.55	2.74	1.55	3.44	1.5 ±0.1	3.37 ±0.05
T	0.53	2.56	0.55	2.58	1.56	3.32	1.5 ±0.1	3.25 ±0.05
TW	0.53	2.56	0.56	2.58	1.54	3.33	1.5 ±0.1	3.25 ±0.05
E[^]	0.52	2.72	0.51	2.74	1.58	3.50	1.5 ±0.1	3.44 ±0.05
TW₂	0.53	2.55	0.56	2.58	1.49	3.23	1.5 ±0.1	3.17 ±0.06
T[^]W₂	0.51	2.55	0.53	2.56	1.48	3.24	1.4 ±0.1	3.17 ±0.06

97

98 The following abbreviations refer to the various tested method options: **B** for baseline eMLR with no
 99 modifications [e.g. Friis *et al.*, 2005]; **E** for ensemble eMLR [Carter *et al.*, 2017]; **T** for the dual-decade
 100 fit proposed by Thacker [2012] and used in this study; * for any variant with C* as a coordinate instead of
 101 DIC [Clement and Gruber, 2018]; & for any variant where the 108/106 times the N* anomaly adjustment
 102 proposed by [Sabine *et al.*, 2002] is also included to account for the potential influences of denitrification;
 103 ^ for two variants where only the first C* adjustment is applied (i.e. where the AOU adjustment is used
 104 without the A_T adjustment or the N* adjustment: this coordinate is used in the manuscript);^X where a
 105 variant on C* is used calculated using a different remineralization ratio (C:O:N = 106:-138:16) than what
 106 was used in the model simulation (C:O:N = 117:-170:15.5), thus representing the impacts of errors in the
 107 assumed remineralization ratios; **W** for a variant where the ensemble members were weighted by inverse
 108 ensemble member misfit; and **W₂** for a variant where the ensemble members were weighted by the
 109 deviation of the C_{anth} accumulation rate term, as is done in this study. Versions that do not use any variant
 110 on C* have an additional term applied that subtracts off 117/170 times a change in the AOU determined
 111 using eMLR or the dual-decade regression [Sabine *et al.*, 2008]. This adjustment was found by Carter *et*
 112 *al.* [2017a] to improve the results from ensemble members that do not include AOU as a predictor.
 113 Switching to C* coordinates involves making an oxygen-dependent adjustment, so this subsequent AOU
 114 adjustment is left out.

115

116 Several lessons are learned by comparing the errors from these runs:

- 117 1. We confirm a conclusion found by Carter *et al.* [2017b], that using the ensemble approach reduces
 118 the overall eMLR bias and RMSE (by 16% and 23%, respectively, comparing **E** vs. **B**).
- 119 2. While using a C* or similar coordinate reduces the methodological error (i.e. the first two columns
 120 of Table S2) up to an additional 56% and 16%, respectively (e.g. **E[^]**, **E***, **E[&]** vs. **E**), it also makes
 121 the estimates more susceptible to cruise offset errors (increasing bias in the rightmost columns of
 122 Table S2 by ~22% for the same comparison). This is because offsets in the various terms used to
 123 calculate the C* variant used (e.g. A_T and AOU for the implementation by Clement and Gruber
 124 [2018]) now affect estimates from all ensemble members regardless of whether the ensemble
 125 members included those predictor parameters. We find that the best approach uses C[^], which is C*
 126 without the adjustments for carbonate cycling or denitrification. While [Clement and Gruber, 2018]
 127 did not test the impacts of measurement biases on their results, we note their approach would be less
 128 susceptible to measurement biases than ours because they are considering changes across many

- 129 cruises at once, with each cruise having its own independent (and perhaps compensating)
130 measurement biases. Also, by including A_T and phosphate in their ensemble members, their
131 estimates will include some of the impacts of these measurement biases already.
- 132 3. The E^X trials applying a different remineralization ratio than the one used in the model simulation
133 showed essentially identical bias to the E^* trials, suggesting eMLR regression coefficients can
134 remove much of the impact of variability that is not accounted for by the choice of coordinates.
 - 135 4. The multi-occupation regression suggested by *Thacker* [2012], has little impact on the mean bias
136 (with our implementation), but leads to a slight, yet statistically significant (4%), reduction of RMS
137 errors (T vs. E). We reiterate that this multi-decade approach has the additional benefit of allowing
138 multiple sections to be used together easily and without re-gridding data or regression coefficients,
139 so we adopt this approach partially out of convenience. We do not assess the added benefit from
140 potentially having 3 cruises in each regression, each with independent and possibly partially
141 cancelling measurement biases.
 - 142 5. Weighting the ensemble members using inverse RMS misfits improved neither AAB nor RMSE
143 significantly in these trials (W vs. E). Weighting by C_{anth} accumulation rate term standard error (i.e.
144 TW_2^* , TW_2^A , and TW_2) resulted in significant (1 to 4%) improvement in the bias and RMSE of the
145 T trials.
 - 146 6. Simulations with added biases were worse when random offsets were not also added (i.e. the AAB
147 and the RMSE of the “systematic errors only” columns are 5% and 2% higher, respectively). This
148 suggests that adding the random measurement noise is effecting a Ridge Regression, and thereby
149 improving the errors from an over-fit signal. Based on this observation, we recommend using a
150 regression approach or a weighting term that responds to overfitting (e.g. our weighting term,
151 weighting by Akaike Information Criteria, or using Ridge Regression), particularly when
152 considering regressions with more predictors than the 3 to 7 we include.

153
154 A separate set of 35 trials using no latitude cutoff for data selection (i.e. with infinitely wide windows)
155 increased the bias by only 1% and the RMS error by 3% compared to similar methods applied to the same
156 35 trials. While we did not opt to use infinitely wide windows, doing so can greatly speed the analysis
157 since regressions need only be fit once per density surface. It may therefore be a worthwhile approach for
158 future variants on this method. In these same 35 trials, variants were also tested in which all data were
159 used for regressions, but the data were weighted with a similar weighting function to Equation 4.
160 However, these regressions had 10% and 7% higher bias and RMSE, respectively, so these weighted
161 methods were not adopted or tested further.

162
163 Based on this analysis, uncertainties in the main body of this paper are propagated assuming standard
164 biases of $1.4 \mu\text{mol kg}^{-1}$ for column inventories and random errors of $3.17 \mu\text{mol kg}^{-1}$ for individual
165 estimates (divided by the time span for rate uncertainties). These estimates apply to the approach
166 generally, but the error from ensemble approach varies regionally and with depth [*Carter et al.*, 2017].
167 We therefore tailor these general estimates for the accumulation rate estimates by separating the
168 methodological bias and RMSE owing to measurement uncertainties from the ensemble member
169 variability. Measurement uncertainty error is calculated as the error estimates without simulated errors
170 (i.e. the first two values in the bottom row of Table S2) subtracted in quadrature from the error estimates
171 with simulated errors (i.e. the rightmost values on the bottom row). These error estimates are then added
172 in quadrature to the standard deviation of the ensemble member estimates obtained throughout the
173 analysis to obtain regionally varying C_{anth} accumulation estimate uncertainties. Only the standard bias
174 integrated over 1100 m is considered for column inventory estimates.

175
176 Uncertainties in the basin inventories are predominately due to $5 \mu\text{mol kg}^{-1}$ (bias) uncertainties in the
177 baseline 1994 estimates taken from *Sabine et al.* [2002], while uncertainties in the decadal increases are
178 derived from the assumption that the average absolute $1.4 \mu\text{mol kg}^{-1}$ estimate biases from the 14 sections
179 are independent and have nearly equal impacts on the final estimates. As discussed in section 3.4, the bias

180 in the LIR reconstructions of C_{anth} accumulations is small. These uncertainties are scaled down for regions
181 (e.g. Table 2) based on the fraction of the overall Pacific volume (above 1500 m depth) represented by the
182 region, but also scaled up to account for having fewer independent sections in an area vs. the whole basin.
183 The uncertainties for the change in the decadal accumulation between decades is propagated assuming the
184 uncertainties in the individual decadal accumulations are independent.

185
186 Biases are significantly lower when measurement errors are excluded (Table S2), suggesting both that
187 biases from errors in assumptions have a small impact on basin inventory change estimates and that
188 measurement uncertainties remain a major contributor to CAREER and other eMLR estimate
189 uncertainties. This suggests a continued strong focus on interior ocean hydrographic measurement quality
190 is critical for continued future C_{anth} monitoring with DIC measurements.

191
192 There are some locations where small but significant negative C_{anth} accumulation rates are estimated at
193 depth (e.g. Fig. 2f). These collectively represent the quantity of spurious negative estimates that would be
194 expected at 95% confidence. Given that these negative estimates should be balanced by a comparable
195 amount of spuriously positive estimates elsewhere (e.g. P01 from 1999 to 2007 at depth, Fig.S2a), they
196 are retained to avoid biasing basin scale changes.

197

198 **Text S2**

199 This is a list of steps taken for the CAREER approach estimates, and is supplemental to the manuscript.

200 Throughout these steps we make frequent use of scaling factors that relate changes in latitude/longitude to
201 changes one another and depth. These scaling factors are only used for selecting which three “nearest”
202 nodes are selected when linearly interpolating between data from one set of scattered observations along a
203 section to another, or between densely gridded 3D data fields. They have no additional impact on the
204 linear interpolation. The scaling factors in the C_{anth} LIR fitting step are exceptions, and this step has a
205 weighting function detailed in the main manuscript.

206 Below we outline the steps involved:

- 207 1. Ingest data
 - 208 a. Extract older data from data products
 - 209 b. Omit data flagged bad or questionable
 - 210 c. Switch to consistent nitrate formulation (nitrate + nitrite)
 - 211 d. Calculate potential density, AOU, depth (sw package, Matlab)
 - 212 e. Manually assign “zonal” or “meridional” to each cruise
 - 213 f. Calculate cruise “decimal year” for each data point
- 214 2. Omit data from stations without corresponding stations in earlier/later occupations
 - 215 a. List stations
 - 216 b. Limit list to unique station locations
 - 217 c. Calculate minimum (great circle route) distances between each station and all other
218 stations in earlier and later corresponding cruises
 - 219 d. Eliminate stations that exceed the lat/lon range of the other corresponding cruises
 - 220 e. Eliminate stations that are too distant from corresponding stations (>120 nautical miles)
- 221 3. Calculate cruise-to-cruise offsets (optional, but useful for QC)
 - 222 a. Use pchip (piecewise cubic Hermite polynomial) interpolation vertically to interpolate
223 earlier and later cruises onto consistent data grids (depths spanning 2500 m to 4000 m at
224 125 m increments).
 - 225 b. Omit pchip extrapolations and interpolations between points that are more than (200 +
226 Depth/5) m apart.

- 227 c. Use Delaunay triangulation to accomplish a 2D interpolation of properties in recent data
- 228 set to depths spanning 2500 m to 4000 m at 125 m increments at latitudes (meridional) or
- 229 longitudes (zonal) (remaining after step 2) in the earlier cruise (Using a latitude/longitude
- 230 to depth conversion of 50 meters per degree to allow a somewhat reasonable point
- 231 selection for interpolation near topography. This number is somewhat arbitrary, but
- 232 unimportant if you already vertically interpolated onto a uniform depth grid.)
- 233 d. Linearly interpolate “cruise bottom depth” along each cruise
- 234 e. omit interpolations located below topography
- 235 f. compute and average point-to-point offsets and multipliers
- 236 g. preserve this information for reference, and consider whether any cruises should be
- 237 examined more closely or omitted (e.g. based on this information P17N was omitted from
- 238 this analysis)
- 239

Table S3. Constant terms used for each of the 16 regressions.

Reg. #	α_1	α_S	α_θ	α_{AOU}	α_N	α_{Si}	α_Y
1	✓	✓	✓	✓	✓	✓	✓
2	✓	✓	✓		✓	✓	✓
3	✓	✓	✓	✓		✓	✓
4	✓	✓	✓			✓	✓
5	✓	✓	✓	✓	✓		✓
6	✓	✓	✓		✓		✓
7	✓	✓	✓	✓			✓
8	✓	✓	✓				✓
9	✓	✓		✓	✓	✓	✓
10	✓	✓			✓	✓	✓
11	✓	✓		✓		✓	✓
12	✓	✓				✓	✓
13	✓	✓		✓	✓		✓
14	✓	✓			✓		✓
15	✓	✓		✓			✓
16	✓	✓					✓

240

- 241 4. Perform the regressions
- 242 a. Iterate over all data locations (regression coordinates) in the second data set (excluding
- 243 data omitted in step 2)
- 244 i. Subset 2 or more datasets for data using the provided lat/lon/depth/density
- 245 windows centered on the regression coordinates (and potential densities)
- 246 ii. Perform 16 robust regressions (using given tuning parameters) relating C^* or C^\wedge
- 247 to the 16 combinations of predictor properties specified (Table S3)
- 248 iii. Output and record the coefficient assigned to the decimal year and its standard
- 249 uncertainty
- 250 5. Override shallow values with assumption of atmospheric equilibration
- 251 a. Interpolate the Holte et al. mixed layer depth climatology to each station in each
- 252 comparison using 2-d latitude and longitude interpolation. Set interpolated values <50 m
- 253 to 50.
- 254 b. For any missing value of alkalinity, silicate, and phosphate, assign a plausible value (we
- 255 used the LIR versions from July 31st 2018 for these estimates
- 256 <https://github.com/BRCScienceProducts/LIRs/commits?author=BRCScienceProducts>).
- 257 Large errors in these estimates translate into small errors in the critical calculation.

- 258 c. Interpolate the Cape Grim atmospheric xCO₂ record to the decimal year of the earlier and
259 the more recent cruises in each comparison
- 260 d. Calculate the DIC expected for the xCO₂ from both the earliest and most recent cruises
261 using the observed/estimated seawater property values from the earliest cruise in the
262 comparisons
- 263 e. Calculate the accumulation rate for each data point in the earliest cruise data set as the
264 difference between these DIC estimates (recent – earlier) divided by the difference in the
265 decimal years of the cruises (recent minus earlier)
- 266 f. Override the subset of measurements found shallower than the modified interpolated
267 mixed layer depth with these values
- 268 6. Combine the regressions
- 269 a. Calculate weights for each decimal year regression coefficients as the inverse of the
270 standard uncertainty on the coefficients
- 271 b. Perform a weighted average for each point of all 16 decimal year regression coefficients
- 272 c. Compute the unweighted standard deviation of ensemble estimates
- 273 i. When plotting, this is added in quadrature with an estimate of the methodological
274 uncertainty for a local estimate of ensemble variability
- 275 7. Interpolate gridded ΔC*-based C_{anth} estimates from the GLODAP version 1 gridded product to
276 the measurement locations.
- 277 a. Subset the gridded data product for the ocean basin you are working in to avoid
278 interpolating across land masses. (We further removed data from the polygon: Lon (deg
279 E)/Lat (deg N) [279.05 8.47;254.83 24.57;271.71 26.28;283.56 10.84;279.05 8.47] where
280 we there seemed to be gridding errors in the 1994 C_{anth} data product.)
- 281 b. Perform 3-D triangulation onto the accumulation rate locations after scaling latitude
282 differences by a factor of 4 and depth differences by a factor of 1/10th
- 283 c. Add the accumulation rates multiplied by (decimal years of the sections-1994).
- 284 i. If multiple rates are being used along a single section, iteratively re-interpolate
285 C_{anth} onto the measurement locations in the earlier data set of each comparison,
286 then add the new rate times the (decimal year of the later section – decimal year
287 of the earlier section) to obtain C_{anth} estimates for successive cruises. Also record
288 the 1995, 2005, and 2015 values for plotting purposes.
- 289 d. Calculate in situ pH and Ω at each data location from observed DIC.
- 290 e. Recalculate these quantities after subtracting C_{anth} from the observed DIC
- 291 f. Calculate the impacts of ocean acidification as the differences (recent minus
292 preindustrial) of these calculated values
- 293 8. Calculate LIR for C_{anth} (details in Section 3.4)
- 294 a. Determine a grid of regression coefficient locations (see Carter et al., 2017 for our
295 default), this is then subset for the Pacific Ocean only
- 296 b. Subset the C_{anth} estimates by the windows given
- 297 c. Weight the properties and the C_{anth} values by the weights given in the manuscript
- 298 d. Use robust regression to regress estimated C_{anth} against the properties indicated
- 299 e. Record the regression coefficients for each gridded location
- 300 9. Use LIR to estimate C_{anth} on the World Ocean Atlas (WOA) grid
- 301 a. Use interpolated regression coefficients with WOA properties to generate C_{anth} estimates
302 at each location in the Pacific portion of the WOA. (See Carter et al., 2017 for our
303 interpolation procedure.)
- 304 b. Use WOA properties to calculate density and WOA grid definition to calculate grid cell
305 volume as (60 nautical miles per degree*1852 meters per nautical mile)² *cos(latitude)
306 *grid-cell-thickness-in-meters (less the portion of the thickness that extends below 1500
307 m)
- 308 c. Multiply C_{anth} estimates by grid cell volumes (in m³) and densities (kg m⁻³)

309 d. Sum along the desired dimensions for the top 1500 m, multiply by 12.01 grams C mol⁻¹
310 CO₂, divide by 1,000,000 μmol mol⁻¹, divide by 10¹⁵ Pg g⁻¹.

311 **Text S3: Steady state circulation model methods**

312 We use two strategies for estimating the C_{anth} accumulation that would be expected under constant
313 circulation. First, we adapt *Gruber et al.* [2019a]'s finding that steady state circulation would lead to an
314 28% C_{anth} increase every 13 years to a 20.9% increase every 10 years, implying ~1.8 PgC more would be
315 taken up in our later decade than our earlier decade, with smaller increases estimated for regional C_{anth}
316 accumulation changes. Second, we use an offline 3-D circulation model simulation [*Khatiwalala*, 2007] of
317 the oceanic DIC response to atmospheric CO₂ increases from the global annual Institute for Atmospheric
318 and Climate Science data product (simulation details are in Supplementary Materials S3). In the steady
319 ocean circulation model's response to the atmospheric pCO₂ changes, Pacific Basin accumulation
320 between 2005 and 2015 increased by 0.9 PgC relative to the preceding decade, i.e. 2.0 PgC less than
321 indicated by the DIC data analysis using CAREER. To arrive at a single accumulation increase estimate,
322 we average these two estimates and use half of the range as a standard uncertainty. Additional details for
323 the second calculation follow.

324 We used a 2.8° by 2.8° transport matrix to simulate ocean circulation (currently hosted by:
325 <https://www.ldeo.columbia.edu/~spk/Research/TMM/tmm.html>). Seawater *T*, *S*, *A_T*, *Si*, and *P* were taken
326 from the gridded GLODAPv2 data product [*Lauvset et al.*, 2016] and re-gridded onto the transport matrix
327 grid using the same gridding procedure used in step 7 in Supplementary Materials S2 (excepting that no
328 data was omitted). These seawater properties were then assumed to be fixed for the duration of the
329 simulation. The simulation then proceeded from 1801 to 2015. On the first time step of each year, the top
330 grid cell (~50 m) of the ocean was assumed to be completely ventilated with respect to a changing
331 atmospheric xCO₂ taken from years 1801 to 2015 of the yearly Institute for Atmospheric and Climate
332 Science data set (as currently linked here: <https://www.co2.earth/historical-co2-datasets>, and the 2015
333 value used the difference between the annual average 2015 and 2014 values in the Mauna Loa data set
334 added to the 2014 value in the IAC data set). In these surface grid cells, a C_{anth} tracer was set equal to the
335 DIC calculated for these grid cells with a 280 ppm atmosphere subtracted from the DIC calculated with
336 the global annual average xCO₂ for that simulation year. For the remainder of the year, this tracer was
337 allowed to passively circulate according the transport matrix, scaled up for 6-hour time steps.

338 This approach significantly overestimates C_{anth} relative to literature estimates, so all estimates are scaled
339 by the ratio of the C_{anth} content we estimate in 1995 (ratio = 0.447) divided by the C_{anth} content simulated
340 in that year. The overestimation is due to deeper C_{anth} penetration in this coarse-resolution long-time-
341 scaled transport matrix (mean penetration depth of 605±3 (1σ) m after 1960) in the simulation than is
342 observed. While the simulated C_{anth} inventory is broadly too large due to deep ventilation, these
343 estimates—once scaled (Fig. S31a)—are thought to provide a reasonable estimate of how much more
344 C_{anth} would be expected in 2005 than 1995 and in 2015 than 2005 simply due to atmospheric CO₂
345 changes. This simple simulation also demonstrates that a linear fit between C_{anth} inventory and
346 atmospheric xCO₂ can be a viable simplification after ~1950 in the absence of significant variability in
347 circulation patterns (Fig. S1), even with potential circulation-induced (or other natural) variability in the
348 xCO₂ records.

349 Similar to *Ríos et al.* [2012], we fit a line relating the atmospheric CO₂ perturbation (xCO₂ at Cape Grim
350 Tasmania) to the Pacific basin inventory above 1500 m depth estimated for 1995, 2005, and 2015 (R² of
351 0.998, p=0.03):

$$352 \text{ Pacific Inventory [PgC]} = 0.5263x\text{CO}_2 - 146.8 \quad (4)$$

353 As in the main paper, Cape Grim is used here because it seems a more appropriate record than
354 alternatives due to the lopsided distribution of the global ocean toward the Southern Hemisphere
355 (particularly the thermocline-ventilating portions of the ocean). This choice has small impact on our

356 results here and for the calculations in section 3.3 however; similar coefficients of 0.5118 and -142.8,
 357 respectively are obtained using the Mauna Loa $x\text{CO}_2$ record. The largest uncertainty in this fit (± 5 PgC)
 358 applies to the constant term and stems from the assumed 1994 reference C_{anth} estimates, however, our
 359 analysis also shows that decadal C_{anth} storage variability can lead to further deviations of at least ± 2 PgC
 360 from the fit.
 361

362 **Supplemental figures**

363

364

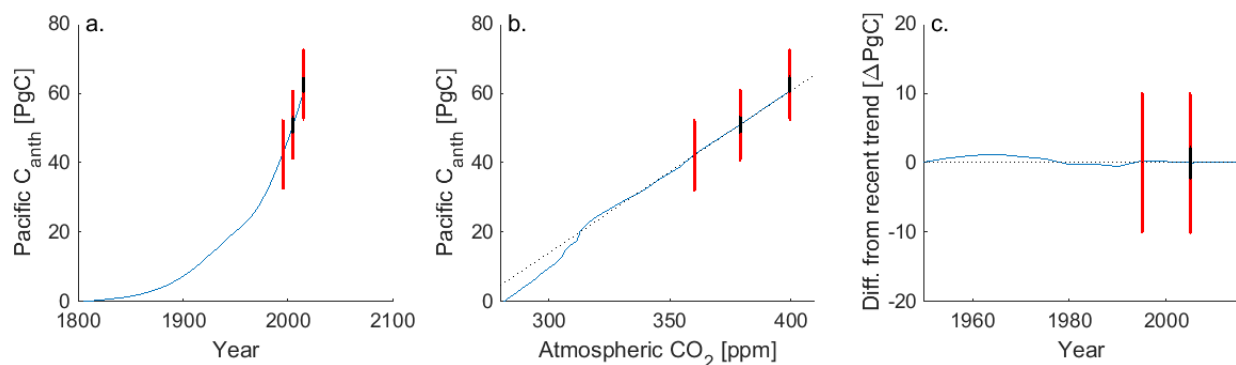
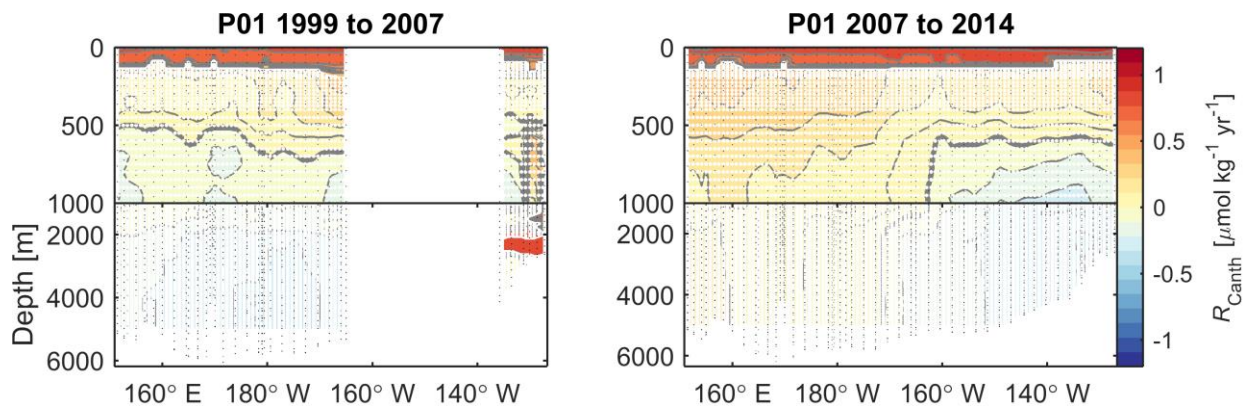


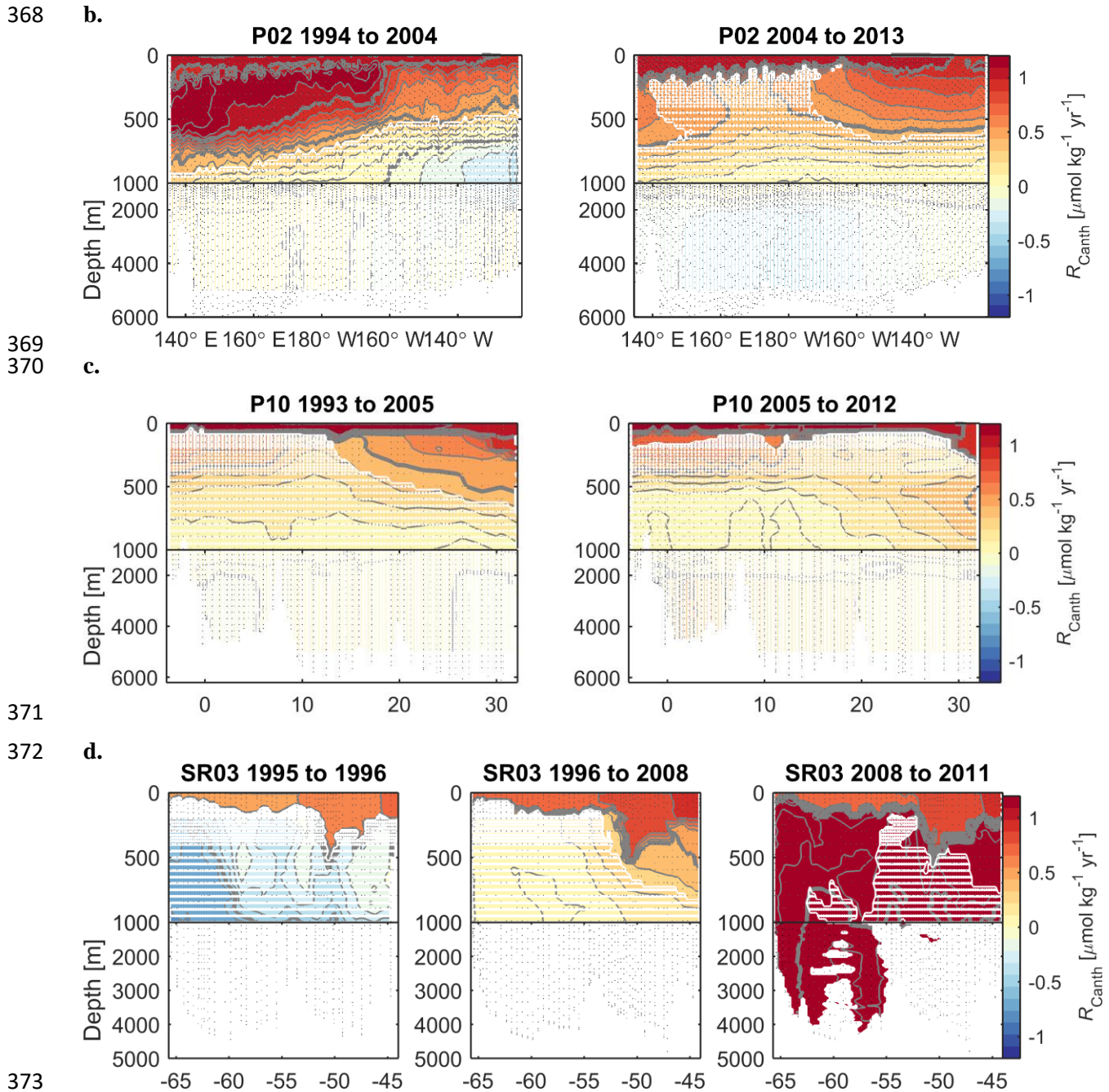
Figure S1 Simulations of Pacific C_{anth} inventory from a transport matrix simulation with fixed circulation plotted as a blue line against (a.) the simulation year and (b.) the atmospheric $p\text{CO}_2$ assumed for each year. In (c.) the difference is plotted between the C_{anth} inventory and a (black dotted) line fit to the last 40 years of data from (b.). Red lines indicate the 95% confidence intervals on the Pacific inventory, and black lines indicate 95% confidence intervals on the differences between the inventories in each decade compared to the decade before. It can be seen that the accumulation during the 2005 to 2015 decade is above, but within uncertainties of, the trend line fit since 1965 in (b.).

365

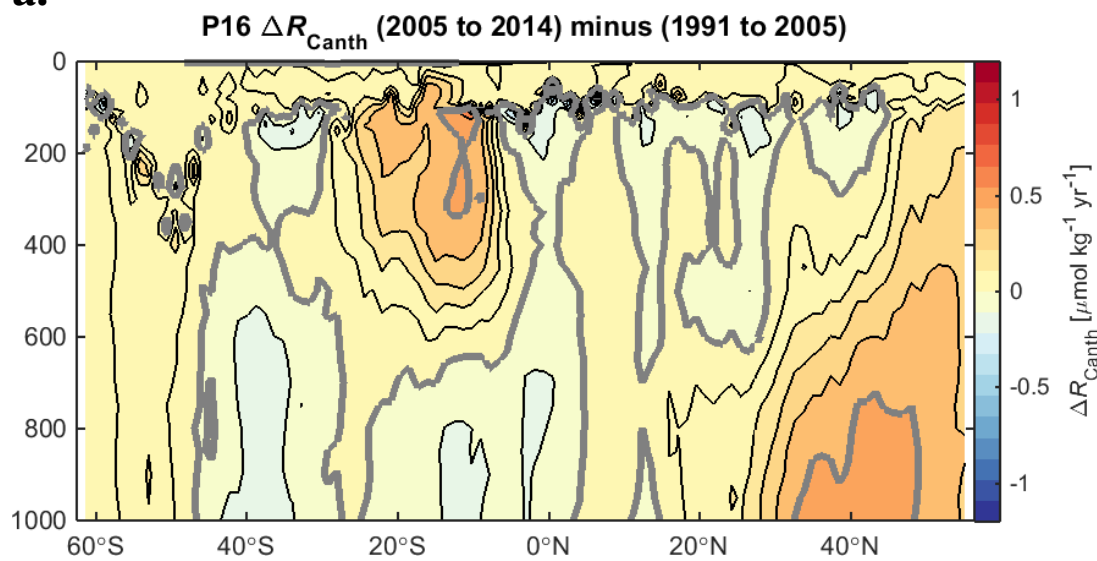
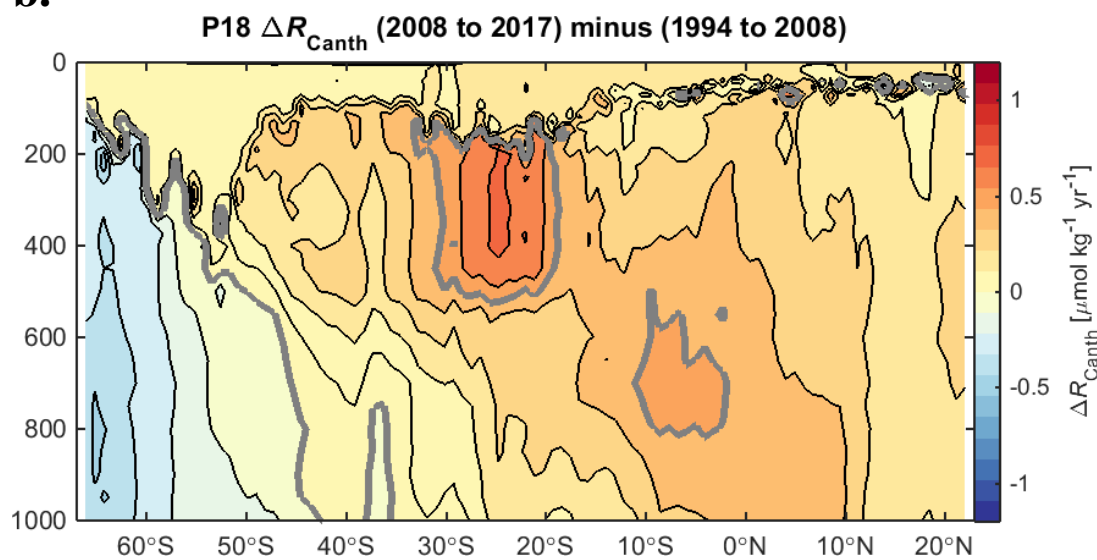
366 a.

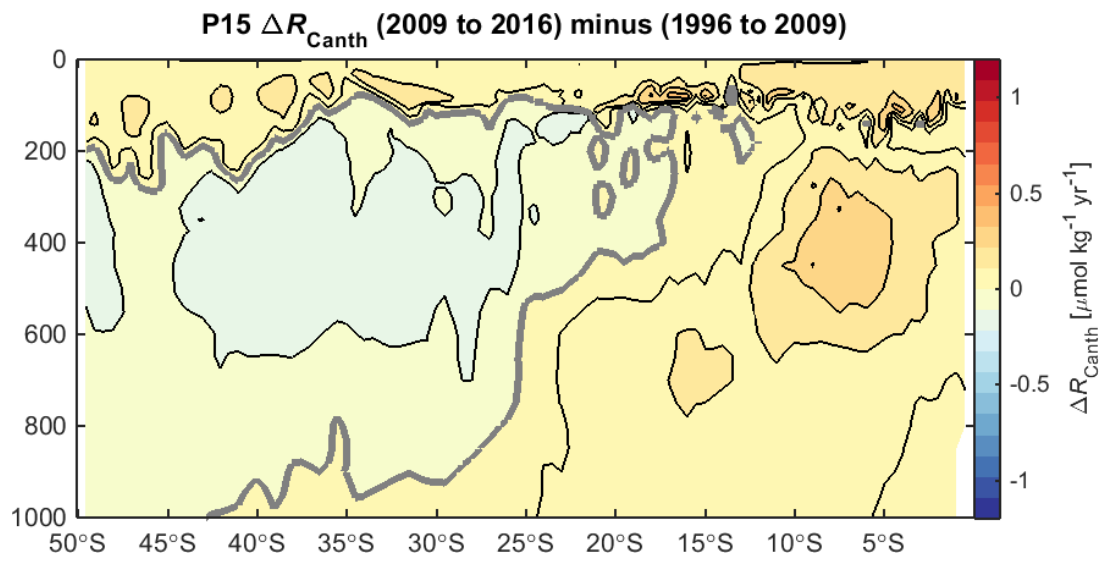


367

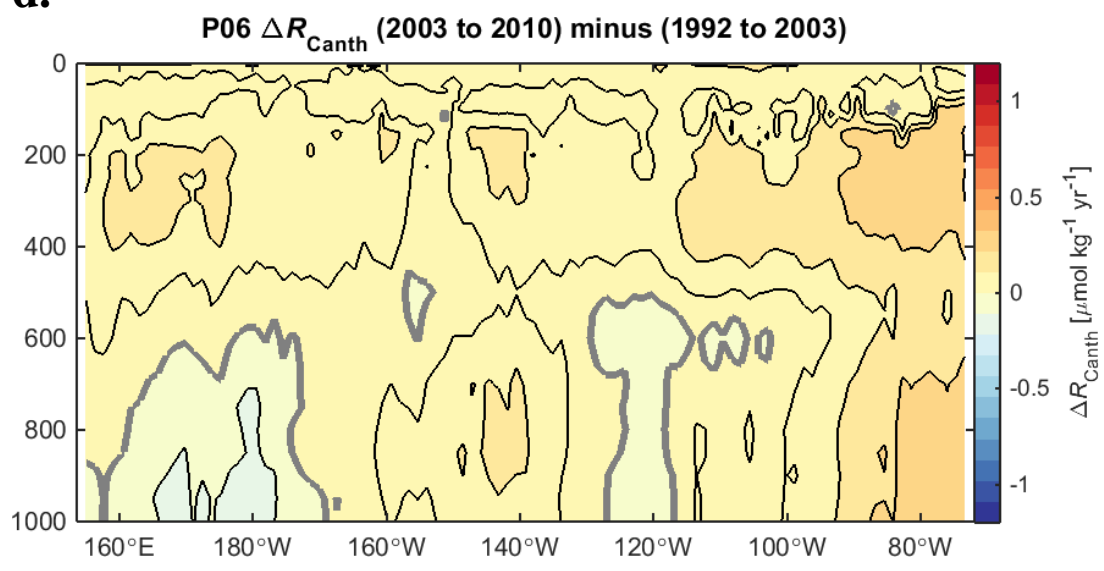


374 **Figure S2.** The remaining successive-occupation accumulation rate estimates not highlighted in the
 375 manuscript. The sections are specified in the panel titles. Insignificant rate changes are obscured by
 376 white dots. The high variability in the SR03 panels (d.) primarily reflects the high relative uncertainty of
 377 successive-occupation estimates for such short time spans. Contours are provided every 0.1 (thin grey)
 378 and 0.5 (thick grey) $\mu\text{mol kg}^{-1} \text{yr}^{-1}$.
 379

a.**b.****c.**



d.



e.

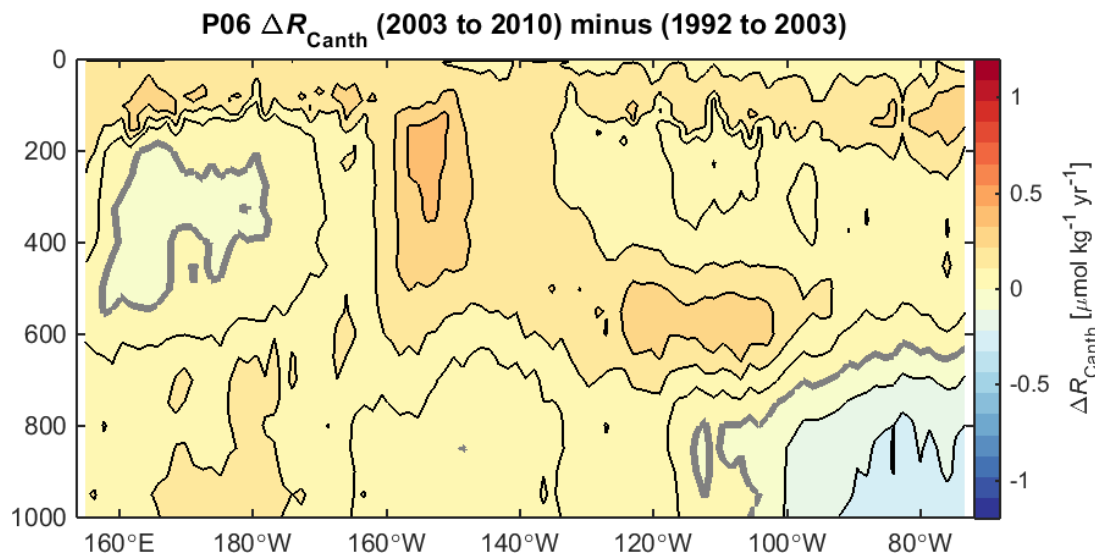


Figure S3. Differences between successive occupation accumulation rates from successive decades for the sections considered in Fig. 7. Contours are provided every 0.1 (thin grey) and 0.5 (thick grey) $\mu\text{mol kg}^{-1} \text{yr}^{-1}$.

381
382

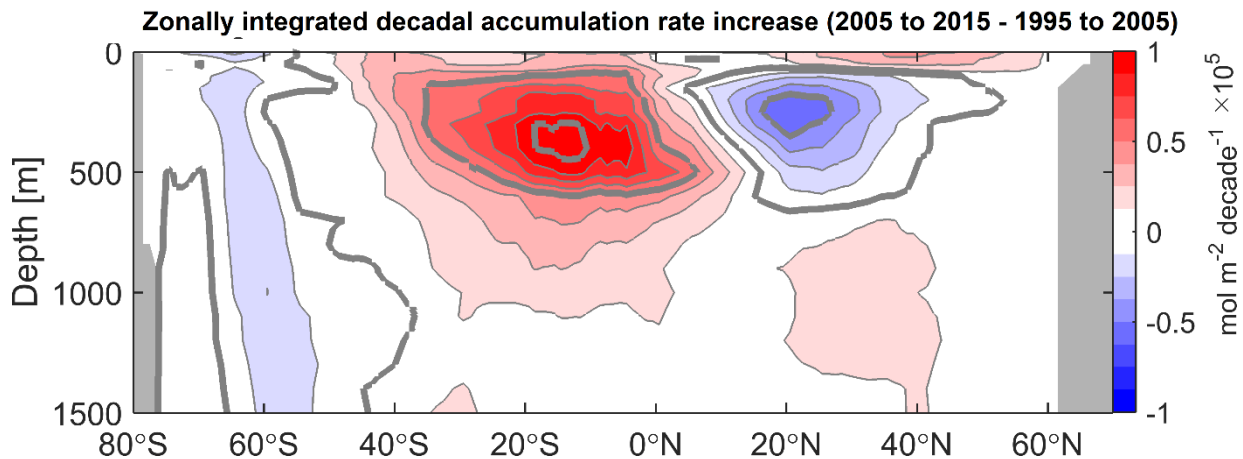
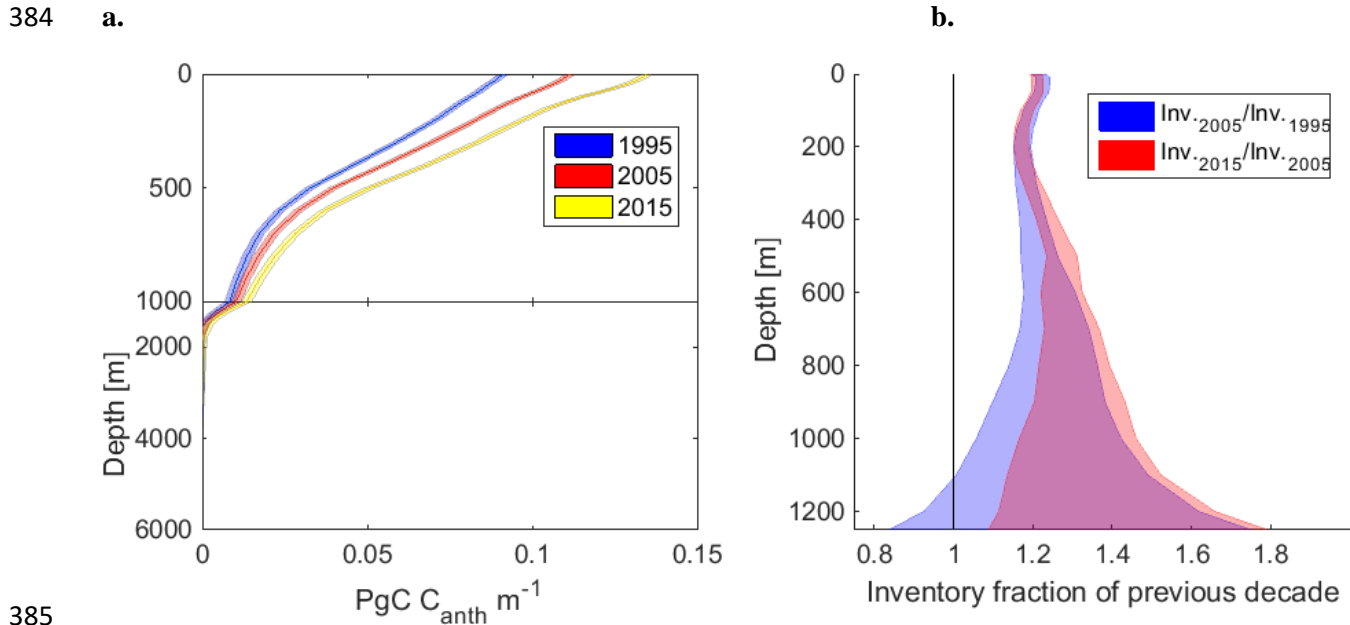


Figure S4. Zonally-integrated basin-inventory accumulation rate changes for the period from 2005 to 2015 relative to the period from 1995 to 2005.

383



386 **Figure S5.** (a.) The vertical distribution of Pacific Basin C_{anth} inventory increases in 1995 (blue), 2005
 387 (red), and 2015 (yellow), and (b.) the ratio of the inventories in each successive decades. Colored areas
 388 represent 1 σ uncertainty intervals. The widening of the ratio near the bottom of (b.) is due to the
 389 consistent uncertainty with a smaller signal at depth.

- 390
- 391 **Movie S1.**
 392 Overall C_{anth} interpolated/extrapolated in time for 1995 through 2017 along all 14 sections considered
 393 across the Pacific.
- 394
- 395 **Movie S2.**
 396 The impact of overall C_{anth} on pH (Δ pH) interpolated/extrapolated in time for 1995 through 2017 along all
 397 14 sections considered across the Pacific.
- 398
- 399 **Movie S3.**
 400 The impact of overall C_{anth} on aragonite saturation state Ω ($\Delta\Omega$) interpolated/extrapolated in time for 1995
 401 through 2017 along all 14 sections considered across the Pacific.

402

403 **Supplement References**

- 404 Carter, B. R. et al. (2017), Two decades of Pacific anthropogenic carbon storage and ocean acidification
 405 along Global Ocean Ship-based Hydrographic Investigations Program sections P16 and P02, *Global*
 406 *Biogeochem. Cycles*, 31(2), 306–327, doi:10.1002/2016GB005485.
- 407 Clement, D., and N. Gruber (2018), The eMLR(C*) method to determine decadal changes in the global
 408 ocean storage of anthropogenic CO₂, *Global Biogeochem. Cycles*, doi:10.1002/2017GB005819.
- 409 Dunne, J. P. et al. (2012), GFDL’s ESM2 Global Coupled Climate–Carbon Earth System Models. Part I:
 410 Physical Formulation and Baseline Simulation Characteristics, *J. Clim.*, 25(19), 6646–6665,
 411 doi:10.1175/JCLI-D-11-00560.1.
- 412 Dunne, J. P. et al. (2013), GFDL’s ESM2 Global Coupled Climate–Carbon Earth System Models. Part II:
 413 Carbon System Formulation and Baseline Simulation Characteristics, *J. Clim.*, 26(7), 2247–2267,
 414 doi:10.1175/JCLI-D-12-00150.1.
- 415 Friis, K., A. Körtzinger, J. Pätsch, and D. W. R. Wallace (2005), On the temporal increase of

416 anthropogenic CO_2 in the subpolar North Atlantic, *Deep Sea Res. Part I Oceanogr. Res. Pap.*, 52(5),
417 681–698, doi:10.1016/j.dsr.2004.11.017.

418 Gruber, N. et al. (2019), The oceanic sink for anthropogenic CO_2 from 1994 to 2007, *Science* (80-.),
419 363(6432), 1193–1199, doi:10.1126/SCIENCE.AAU5153.

420 Key, R. M. et al. (2010), The CARINA data synthesis project: introduction and overview, *Earth Syst. Sci.*
421 *Data*, 2(1), 105–121, doi:10.5194/essd-2-105-2010.

422 Khatiwala, S. (2007), A computational framework for simulation of biogeochemical tracers in the ocean,
423 *Global Biogeochem. Cycles*, 21(3), 1–14, doi:10.1029/2007GB002923.

424 Lauvset, S. K. et al. (2016), A new global interior ocean mapped climatology: the $1^\circ \times 1^\circ$ GLODAP
425 version 2, *Earth Syst. Sci. Data*, 8(2), 325–340, doi:10.5194/ESSD-8-325-2016.

426 Olsen, A. et al. (2016), The Global Ocean Data Analysis Project version 2 (GLODAPv2) – an internally
427 consistent data product for the world ocean, *Earth Syst. Sci. Data*, 8(2), 297–323, doi:10.5194/essd-
428 8-297-2016.

429 Ríos, A. F., A. Velo, P. C. Pardo, M. Hoppema, and F. F. Pérez (2012), An update of anthropogenic CO_2
430 storage rates in the western South Atlantic basin and the role of Antarctic Bottom Water, *J. Mar.*
431 *Syst.*, 94, 197–203, doi:10.1016/J.JMARSYS.2011.11.023.

432 Sabine, C. L., R. A. Feely, R. M. Key, J. L. Bullister, F. J. Millero, K. Lee, T.-H. Peng, B. Tilbrook, T.
433 Ono, and C. S. Wong (2002), Distribution of anthropogenic CO_2 in the Pacific Ocean, *Global*
434 *Biogeochem. Cycles*, 16(4), 30-1-30–17, doi:10.1029/2001GB001639.

435 Sabine, C. L., R. A. Feely, F. J. Millero, A. G. Dickson, C. Langdon, S. Mecking, and D. Greeley (2008),
436 Decadal changes in Pacific carbon, *J. Geophys. Res.*, 113(C7), C07021, doi:10.1029/2007JC004577.

437 Thacker, W. C. (2012), Regression-based estimates of the rate of accumulation of anthropogenic CO_2 in
438 the ocean: A fresh look, *Mar. Chem.*, 132–133, 44–55, doi:10.1016/J.MARCHEM.2012.02.004.

439